Available online at www.sciencedirect.com
SCIENCE DIRECT®
Journal of Magnetic Resonance 167 (2004) 253–258
JMR Journal of Magnetic Resonance
www.elsevier.com/locate/jmr

Sensitivity-enhanced IPAP experiments for measuring one-bond $^{13}C'$–$^{13}C^{\alpha}$ and $^{13}C^{\alpha}$–$^{1}H^{\alpha}$ residual dipolar couplings in proteins

Keyang Ding and Angela M. Gronenborn*

Laboratory of Chemical Physics, National Institute of Diabetes and Digestive and Kidney Diseases, National Institutes of Health, Bethesda, MD 20892, USA

Received 14 November 2003; revised 23 December 2003

Abstract

Sensitivity-enhanced 2D IPAP experiments using the accordion principle for measuring one-bond $^{13}C'$–$^{13}C^{\alpha}$ and $^{1}H^{\alpha}$–$^{13}C^{\alpha}$ dipolar couplings in proteins are presented. The resolution of the resulting spectra is identical to that of the decoupled HSQC spectra and the sensitivity of the corresponding 1D acquisitions are only slightly lower than those obtained with 3D HNCO and 3D HN(COCA)HA pulse sequences due to an additional delay 2Δ. For cases of limited resolution in the 2D ^{15}N–$^{1}H^{N}$ HSQC spectrum the current pulse sequences can easily be modified into 3D versions by introducing a poorly digitized third dimension, if so desired. The experiments described here are a valuable addition to the suites available for determination of residual dipolar couplings in biological systems.

Keywords: Residual dipolar couplings; IPAP; Sensitivity enhancement; Proteins

1. Introduction

Residual dipolar couplings (RDCs) [1,2] of partially aligned molecules provide important long-range constraints for protein NMR structure determination. The most commonly used five RDCs in proteins are the backbone one-bond ^{15}N–$^{1}H^{N}$, ^{15}N–$^{13}C'$, $^{13}C'$–$^{13}C^{\alpha}$, and $^{1}H^{\alpha}$–$^{13}C^{\alpha}$ and two-bond $^{1}H^{N}$–$^{13}C'$ dipolar couplings [3]. If the 2D ^{15}N–$^{1}H^{N}$ HSQC spectrum is well-resolved, it is relatively easy and straightforward to measure the one-bond ^{15}N–$^{1}H^{N}$, ^{15}N–$^{13}C'$ and two-bond $^{1}H^{N}$–$^{13}C'$ dipolar couplings [4–6]. However, the determination of one-bond $^{13}C'$–$^{13}C^{\alpha}$ and $^{1}H^{\alpha}$–$^{13}C^{\alpha}$ dipolar couplings is more involved and takes considerable measuring time. Frequently it is necessary to record 3D experiments [7–12], even though the values of one-bond $^{13}C'$–$^{13}C^{\alpha}$ and $^{1}H^{\alpha}$–$^{13}C^{\alpha}$ couplings are quite large and the corresponding 2D ^{15}N–$^{1}H^{N}$ HSQC spectrum is well-resolved. It therefore is highly desirable to have optimized experiments available for measuring the latter two couplings in two-dimensional spectra. In this communication, sensitivity-enhanced [13,14] 2D IPAP [15] experiments that use the accordion principle [16,17] are presented. They are ideally suited for the determination of one-bond $^{13}C'$–$^{13}C^{\alpha}$ and $^{1}H^{\alpha}$–$^{13}C^{\alpha}$ dipolar couplings in proteins. Combination of experiments allows one to extract all five of the above listed RDCs in a suite of 2D spectra, provided the corresponding 2D ^{15}N–$^{1}H^{N}$ HSQC spectrum is well-resolved. For highly overlapped cases of 2D ^{15}N–$^{1}H^{N}$ HSQC spectra this suite of 2D experiments can be easily transformed into a 3D suite by introducing a poorly digitized third dimension.

2. Sensitivity-enhanced IPAP experiment for measuring $^{13}C'$–^{13}C couplings

Fig. 1A presents the pulse sequence of the sensitivity-enhanced IPAP experiment for measuring one-bond $^{13}C'$–$^{13}C^{\alpha}$ couplings. The forward and backward ^{15}N–$^{13}C'$ INEPT transfer steps occur in the periods a–b and e–f, respectively. Two alternating π pulses in the $^{13}C^{\alpha}$ channel depicted by the solid and the dashed open bars

* Corresponding author. Fax: 1-301-496-1690.
E-mail address: gronenborn@nih.gov (A.M. Gronenborn).

1090-7807/$ - see front matter © 2004 Elsevier Inc. All rights reserved.
doi:10.1016/j.jmr.2003.12.016

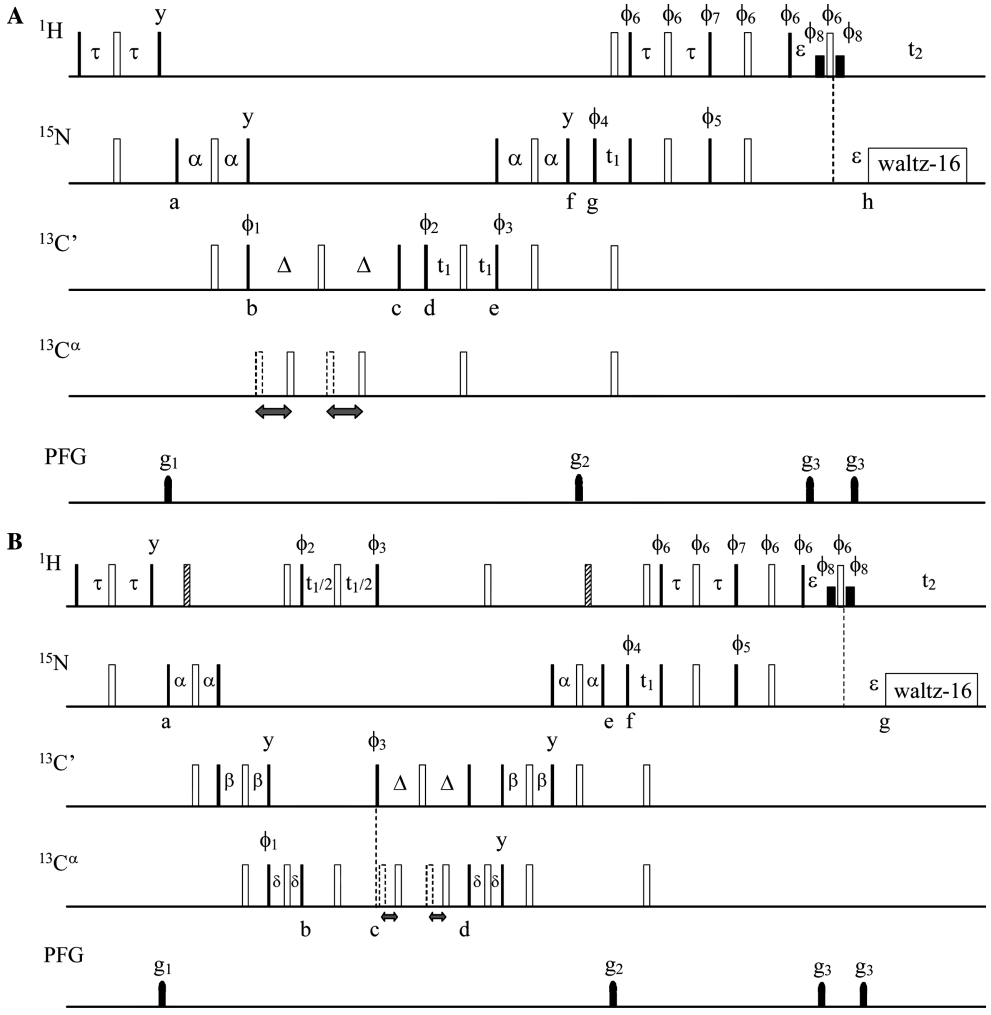

Fig. 1. Pulse sequences of sensitivity-enhanced IPAP experiments for measuring one-bond $^{13}C'$–$^{13}C^{\alpha}$ (A) and $^{13}C^{\alpha}$–$^{1}H^{\alpha}$ (B) residual dipolar couplings. Narrow (filled) and wide (open) bars represent 90° and 180° pulses with phase x, respectively, unless indicated otherwise. Proton 90° soft pulses of 1 ms duration are used for Watergate [18] water suppression and these are depicted by short filled bars. The carrier frequencies in the ^{1}H, ^{15}N, $^{13}C'$, and $^{13}C^{\alpha}$ channels are positioned at 4.7 (water resonance), 118, 177, and 56 ppm, respectively. The power levels for 90° and 180° pulses in the $^{13}C'$ and $^{13}C^{\alpha}$ channels are set at $\Delta\omega_0/(15)^{1/2}$ and $\Delta\omega_0/(3)^{1/2}$, respectively, with $\Delta\omega_0$ being the difference in Hz between the $^{13}C'$ and $^{13}C^{\alpha}$ carrier frequencies. The inter-pulse delays are: $\tau = 2.5$ ms, $\Delta = 4.75$ ms, $\alpha = 12.5$ ms, $\beta = 4.5$ ms, $\delta = 1.7$ ms, and $\varepsilon = 1.5$ ms. The PFG g_1, g_2, and g_3 are sine-shaped with maximal 20 G/cm and durations of 3, 1.5, and 0.6 ms, respectively. For a system with very fast relaxing $2N_xH_z^N$ magnetization, proton decoupling can be used and inserted in the period a–f, starting 2τ after point a and finishing 2τ before point f, by changing the two y-phase pulses in the ^{15}N channel into two x-phase pulses in pulse sequence (A). Two proton-decoupling periods can be implemented to replace the hatched π pulses, starting and ending at the hatched π pulse positions and covering the two 2β periods, respectively, in pulse sequence (B). (A) For the $(4n-3)$th and $(4n-1)$th experiments, the phase cycles are set as: $\phi_1 = x,x,-x,-x$; $\phi_2 = 8(x),8(-x)$; $\phi_3 = x$; and $\phi_4 = x,-x,x,-x,y,-y,y,-y$ in the $(4n-3)$th experiments and $\phi_4 = x,-x,x,-x,-y,y,-y,y$ in the $(4n-1)$th experiments; $\phi_5 = y$ in the $(4n-3)$th experiments and $\phi_5 = -y$ in the $(4n-1)$th experiments; $\phi_6 = 4(x),4(y)$; $\phi_7 = 4(y),4(-x)$; $\phi_8 = 4(-x),4(-y)$; and $\phi_{Rec} = x,-x,-x,x,x,-x,-x,x,-x,x,x,-x,-x,x,x,-x$. For the $(4n-2)$th experiments, a 90° phase increment is set to ϕ_1, ϕ_3, and ϕ_{Rec} with respect to the $(4n-3)$th experiments. For the $(4n)$th experiments, a 90° phase increase is set to ϕ_1 and ϕ_{Rec} and a 90° phase decrease is set to ϕ_3 with respect to the $(4n-1)$th experiments. The $^{13}C^{\alpha}$ π pulses between points b and c are located at the positions of the open bars in the $(4n-3)$th and $(4n-1)$th experiments, while they are shifted to the positions of the dashed bars in the $(4n-2)$th and $(4n)$th experiments. (B) For the $(4n-3)$th and $(4n-1)$th experiments, the phase cycles are set as: $\phi_1 = y,y,-y,-y$; $\phi_2 = 4(x),4(-x)$; $\phi_3 = x$; $\phi_4 = x,-x,x,-x,x,-x,x,-x,y,-y,y,-y,y,-y,y,-y$ in the $(4n-3)$th experiments and $\phi_4 = x,-x,x,-x,x,-x,x,-x,-y,y,-y,y,-y,y,-y,y$ in the $(4n-1)$th experiments; $\phi_5 = y$ in the $(4n-3)$th experiments and $\phi_5 = -y$ in the $(4n-1)$th experiments; $\phi_6 = 8(x),4(y)$; $\phi_7 = 8(y),4(-x)$; $\phi_8 = 8(-x),8(-y)$ and $\phi_{Rec} = x,-x,-x,x,-x,x,x,-x$. For the $(4n-2)$th experiments, a 90° phase increment is set to ϕ_3 and ϕ_{Rec} with respect to the $(4n-3)$th experiments. For the $(4n)$th experiments, a 90° phase increase is set to ϕ_3 and ϕ_{Rec} and a 180° phase decrease is set to ϕ_2 with respect to the $(4n-1)$th experiments. The two proton π pulses shown by hatched bars are applied 2.5 ms after point a and before point e, respectively. The $^{13}C^{\alpha}$ π pulses between points c and d are located at the positions of the open bars in the $(4n-3)$th and $(4n-1)$th experiments, while they are moved to the positions of the dashed bars in the $(4n-2)$th and $(4n)$th experiments.

are inserted between b and c and the $^{13}C'$–$^{13}C^{\alpha}$ coupling J_{CC} evolves during d–e. The two π pulses in the $^{13}C^{\alpha}$ channel at the positions, depicted by open bars, select the $\cos(2\pi J_{CC}t_1)$ term as an amplitude modulation to the detected FID. Alternatively, inserting the two π pulses in the $^{13}C^{\alpha}$ channel at the positions of the dashed open

Table 1
Modulation of the $^{13}C'$–$^{13}C^{\alpha}$ coupling J_{CC} and the ^{15}N chemical shift frequency ω_N of the raw and manipulated FIDs in the 2D series for values of n from 1 to $TD_1/2$

2D series number	Real part	Imaginary part
$4n-3$	$\cos(2\pi J_{CC}t_1)\cos(\omega_H t_2-\omega_N t_1)$	$-\cos(2\pi J_{CC}t_1)\sin(\omega_H t_2-\omega_N t_1)$
$4n-2$	$\sin(2\pi J_{CC}t_1)\sin(\omega_H t_2-\omega_N t_1)$	$\sin(2\pi J_{CC}t_1)\cos(\omega_H t_2-\omega_N t_1)$
$4n-1$	$\cos(2\pi J_{CC}t_1)\cos(\omega_H t_2+\omega_N t_1)$	$-\cos(2\pi J_{CC}t_1)\sin(\omega_H t_2+\omega_N t_1)$
$4n$	$-\sin(2\pi J_{CC}t_1)\sin(\omega_H t_2+\omega_N t_1)$	$\sin(2\pi J_{CC}t_1)\cos(\omega_H t_2+\omega_N t_1)$
$(2n-1)=(4n-3)+(4n-2)$	$\cos[\omega_H t_2-(\omega_N+2\pi J_{CC})t_1]$	$-\sin[\omega_H t_2-(\omega_N+2\pi J_{CC})t_1]$
$2n=(4n-1)+(4n)$	$\cos[\omega_H t_2+(\omega_N+2\pi J_{CC})t_1]$	$-\sin[\omega_H t_2+(\omega_N+2\pi J_{CC})t_1]$
$(2n-1)=(4n-3)-(4n-2)$	$\cos[\omega_H t_2-(\omega_N-2\pi J_{CC})t_1]$	$-\sin[\omega_H t_2-(\omega_N-2\pi J_{CC})t_1]$
$2n=(4n-1)-(4n)$	$\cos[\omega_H t_2+(\omega_N-2\pi J_{CC})t_1]$	$-\sin[\omega_H t_2+(\omega_N-2\pi J_{CC})t_1]$

bars, the $\sin(2\pi J_{CC}t_1)$ term is selected. The segment g–h of the pulse sequence is simply the sensitivity-enhanced ^{15}N–$^{1}H^{N}$ HSQC sequence and the ^{15}N chemical shift evolves as the phase modulation to the detected FID. Table 1 summarizes the modulations of the $^{13}C'$–$^{13}C^{\alpha}$ coupling J_{CC} and the ^{15}N chemical shift frequency ω_N of the raw and manipulated FIDs in the 2D series.

During the period between points b and c, the in-phase magnetization $-4C'_yN_zH^N_z$ decays simply by the $^{13}C'$ transverse relaxation rate compensating for the intensity loss of the anti-phase magnetization during the same period. The anti-phase magnetization $8C'_yC^{\alpha}_zN_zH^N_z$ is generated by using a $^{13}C'$–$^{13}C^{\alpha}$ INEPT transfer step from point b to c with a intensity factor of $\sin(2\pi J_{CC}\Delta)$. As compared to the ^{15}N–$^{1}H^{N}$ couplings, the $^{13}C'$–$^{13}C^{\alpha}$ couplings are more uniform and $\sin(2\pi J_{CC}\Delta)=1$ holds quite accurately. Since the $^{13}C'$–$^{13}C^{\alpha}$ coupling is about the half of the ^{15}N–$^{1}H^{N}$ coupling, a scaling factor of 2 is introduced here for the evolution of the $^{13}C'$–$^{13}C^{\alpha}$ coupling in order to keep the apparent splitting within the same range as in a ^{15}N–$^{1}H^{N}$ IPAP spectrum. Although the introduction of a scaling factor of 2 reduces the sensitivity of the spectrum by broadening the resonance lines, the error in measuring the splitting is also reduced by a factor of 2 when the couplings are calculated from the apparent splittings, dividing the latter by the scaling factor 2. As is shown below (see Fig. 3), a better correlation is obtained for the measured and predicted $^{13}C'$–$^{13}C^{\alpha}$ RDC data compared to the $^{1}H^{\alpha}$–$^{13}C^{\alpha}$ RDC data, although the $^{13}C'$–$^{13}C^{\alpha}$ RDCs are quite small. This suggests that the error in the $^{13}C'$–$^{13}C^{\alpha}$ coupling measurement is small.

As presented in the first four rows of Table 1, the raw dataset consists of $(2TD_1)\times TD_2$ points. The $^{13}C'$–$^{13}C^{\alpha}$ coupling J_{CC} modulates the amplitude of the detected FIDs, while the ^{15}N chemical shift frequency ω_N the initial phase. By adding/subtracting the $(4n-2)$th and $(4n)$th rows to/from the $(4n-3)$th and $(4n-1)$th rows, two new datasets with $TD_1\times TD_2$ points are obtained and these are listed in the two middle rows and the last two rows of Table 1, respectively. By manipulating these new datasets in an echo, anti-echo manner [13,14], 2D Fourier transformation results in two sensitivity-enhanced sub-spectra with the ^{15}N–$^{1}H^{N}$ HSQC cross-peaks located at $(\omega_N+2\pi J_{CC},\ \omega_H)$ and $(\omega_N-2\pi J_{CC},\ \omega_H)$, respectively. Since a scaling factor of 2 is used, half of the displacement along the ^{15}N dimension between these two sub-spectra provides a direct measure for the one-bond $^{13}C'$–$^{13}C^{\alpha}$ couplings.

3. Sensitivity-enhanced IPAP experiment for measuring ^{1}H–^{13}C couplings

Fig. 1B displays the pulse sequence of the sensitivity-enhanced IPAP experiment for measuring the one-bond $^{1}H^{\alpha}$–$^{13}C^{\alpha}$ couplings. Similar to the sequence in Fig. 1A, the a–b and d–e periods contain the forward and backward ^{15}N–$^{13}C'$–$^{13}C^{\alpha}$–$^{1}H^{\alpha}$ INEPT transfer steps, respectively. The $^{1}H^{\alpha}$–$^{13}C^{\alpha}$ coupling J_{CH} evolves in the period b–c. Two π pulses in the $^{13}C^{\alpha}$ channel alternate between the positions depicted by open and dashed bars during c–d for selection of the $\cos(\pi J_{CH}t_1)$ and $\sin(\pi J_{CH}t_1)$ terms. The segment f–g is the sensitivity-enhanced ^{15}N–$^{1}H^{N}$ HSQC sequence. Table 2 summarizes the modulations of the $^{1}H^{\alpha}$–$^{13}C^{\alpha}$ coupling J_{CH} and the ^{15}N chemical shift frequency ω_N to the raw and manipulated FIDs in the 2D series.

From a simple analysis based on the product operator formalism, the magnetization at point b can be expressed as $8H^{\alpha}_yC^{\alpha}_zC'_zN_z$. It evolves into two terms: $8H^{\alpha}_yC^{\alpha}_zC'_zN_z\cos(\pi J_{CH}t_1)$ and $-4H^{\alpha}_xC'_zN_z\sin(\pi J_{CH}t_1)$ at point c. During period between c and d, a $^{13}C'$–$^{13}C^{\alpha}$ INEPT transfer step transforms the $\sin(\pi J_{CH}t_1)$-modulated magnetization into $-8H^{\alpha}_zC^{\alpha}_yC'_zN_z\sin(2\pi J_{CC}\Delta)$. For the $\cos(\pi J_{CH}t_1)$-modulated magnetization $-8H^{\alpha}_zC^{\alpha}_yC'_zN_z$, the period from the point c to d is simply a relaxation delay to compensate for the intensity loss of $\sin(\pi J_{CH}t_1)$-modulated magnetization during that period. Since the $^{13}C'$–$^{13}C^{\alpha}$ couplings are quite uniform, $\sin(2\pi J_{CC}\Delta)=1$ holds almost accurately. This alleviates any problems associated with the very wide range of $^{13}C^{\alpha}$–$^{1}H^{\alpha}$ couplings during the $^{13}C^{\alpha}$–$^{1}H^{\alpha}$ INEPT transfer step [9] that is used to generate the anti-phase magnetization of $^{13}C^{\alpha}$ with respect to $^{1}H^{\alpha}$. In addition, using $^{1}H^{\alpha}$ rather than $^{13}C^{\alpha}$ for the $^{13}C^{\alpha}$–$^{1}H^{\alpha}$ coupling

Table 2
Modulation of the $^{1}H^{\alpha}$–$^{13}C^{\alpha}$ coupling J_{CH} and ^{15}N chemical shift frequency ω_N of the raw and manipulated FIDs in the 2D series for values of n from 1 to $TD_1/2$

2D series number	Real part	Imaginary part
$4n-3$	$\cos(\pi J_{CH}t_1)\cos(\omega_H t_2-\omega_N t_1)$	$-\cos(\pi J_{CH}t_1)\sin(\omega_H t_2-\omega_N t_1)$
$4n-2$	$\sin(\pi J_{CH}t_1)\sin(\omega_H t_2-\omega_N t_1)$	$\sin(\pi J_{CH}t_1)\cos(\omega_H t_2-\omega_N t_1)$
$4n-1$	$\cos(\pi J_{CH}t_1)\cos(\omega_H t_2+\omega_N t_1)$	$-\cos(\pi J_{CH}t_1)\sin(\omega_H t_2+\omega_N t_1)$
$4n$	$-\sin(\pi J_{CH}t_1)\sin(\omega_H t_2+\omega_N t_1)$	$\sin(\pi J_{CH}t_1)\cos(\omega_H t_2+\omega_N t_1)$
$(2n-1)=(4n-3)+(4n-2)$	$\cos[\omega_H t_2-(\omega_N+\pi J_{CH})t_1]$	$-\sin[\omega_H t_2-(\omega_N+\pi J_{CH})t_1]$
$2n=(4n-1)+(4n)$	$\cos[\omega_H t_2+(\omega_N+\pi J_{CH})t_1]$	$-\sin[\omega_H t_2+(\omega_N+\pi J_{CH})t_1]$
$(2n-1)=(4n-3)-(4n-2)$	$\cos[\omega_H t_2-(\omega_N-\pi J_{CH})t_1]$	$-\sin[\omega_H t_2-(\omega_N-\pi J_{CH})t_1]$
$2n=(4n-1)-(4n)$	$\cos[\omega_H t_2+(\omega_N-\pi J_{CH})t_1]$	$-\sin[\omega_H t_2+(\omega_N-\pi J_{CH})t_1]$

evolution has further advantages since it is insignificantly affected by the large homonuclear $^{13}C^{\alpha}$–$^{13}C^{\beta}$ couplings.

The first four rows of Table 2 contain the raw dataset consisting of $(2TD_1)\times TD_2$ points. The $^{1}H^{\alpha}$–$^{13}C^{\alpha}$ coupling J_{CH} amplitude modulates the detected FIDs and the ^{15}N chemical shift frequency ω_N the initial phase. Adding/subtracting the $(4n-2)$th and $(4n)$th rows to/from the $(4n-3)$th and $(4n-1)$th rows, yields two new datasets with $TD_1\times TD_2$ points and these are listed in the two middle rows and the last two rows in Table 2, respectively. Echo, anti-echo manipulation [13,14] of these new datasets, and 2D Fourier transformation results in two sensitivity-enhanced sub-spectra with the

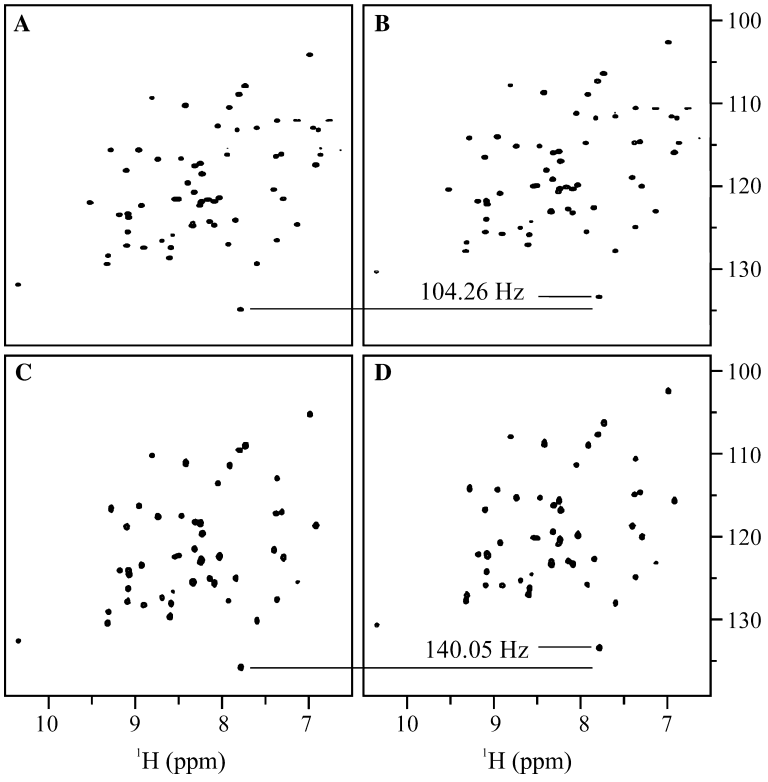

Fig. 2. Experimental IPAP spectra recorded on a sample of ~0.5 mM uniformly ^{13}C,^{15}N-labeled protein GB1, dissolved in liquid crystalline PF1 (15 mg/ml) in 95% H_2O/5% D_2O at pH ≈ 7 using the pulse scheme presented in Fig. 1. The spectra were recorded on a Bruker DMX 600 spectrometer with a ^{1}H frequency of 600.13 MHz. (A) and (B) are the IPAP pair for measuring one-bond $^{13}C'$–$^{13}C^{\alpha}$ couplings, recorded using the pulse sequence in Fig. 1A. Since a scaling factor of 2 was used for the $^{13}C'$–$^{13}C^{\alpha}$ coupling evolution, the displacement in the spectra is two times the coupling value. Other parameters are: 2D spectral widths $SW_1\times SW_2=2500\times 8992.806$ Hz, data points of the raw time domain dataset $2(TD_1\times TD_2)=2(512\times 1024)$, $ns=32$, recycle delay = 1 s. The total experimental time is approximately 9 h. The spectra were processed with the window function of squared sine bell in both dimensions, which consist of 1024×1024 points. (C) and (D) are the IPAP pair for measuring one-bond $^{1}H^{\alpha}$–$^{13}C^{\alpha}$ couplings, recorded using the pulse sequence in Fig. 1B. The coupling value is given by the displacement in these spectra. All other parameters are as listed for the (A) and (B) pair above, except $ns=62$, resulting in a total experiment time of approximately 18 h. All spectra were processed with squared sine bell window functions in both dimensions, consisting of 1024×1024 points. Data processing was carried out using nmrPipe and nmrDraw software [20].

^{15}N–$^{1}H^{N}$ HSQC cross-peaks located at ($\omega_N + \pi J_{CH}$, ω_H) and ($\omega_N - \pi J_{CH}$, ω_H), respectively. The displacement along the ^{15}N dimension between these two sub-spectra provides a direct measure for the one-bond $^{1}H^{\alpha}$–$^{13}C^{\alpha}$ couplings.

4. Results and discussion

The IPAP experiments using the pulse sequences presented above were recorded on a sample of ~0.5 mM uniformly ^{13}C,^{15}N-labeled protein GB1 [19], dissolved in liquid crystalline PF1 (15 mg/ml) in 95% H_2O/5% D_2O at pH ~ 7, and the corresponding dipolar couplings were measured. The experimental spectra displayed in Figs. 2A and B are the IPAP pair for determining one-bond $^{13}C'$–$^{13}C^{\alpha}$ couplings that were recorded using the pulse sequence depicted in Fig. 1A, and Figs. 2C and D the IPAP pair for measuring one-bond $^{1}H^{\alpha}$–$^{13}C^{\alpha}$ couplings using the pulse sequence of Fig. 1B. Since a scaling factor of 2 was used for the evolution of the $^{13}C'$–$^{13}C^{\alpha}$ coupling, the apparent displacement in the (A) and (B) pair of spectra is twice the value of the coupling, whereas in the (C) and (D) pair the displacement is equal to the coupling. All data were processed with nmrPipe and nmrDraw [20].

The correlations between measured and predicted D_{CC} values (A) and D_{CH} values (B) are shown in Fig. 3. RDCs were calculated using the program SSIA [21] based on the refined NMR structure (PDB code: 3GB1) [22] as the model structure. As can be noted, good agreement between experimental and calculated RDCs is observed. For the D_{CC} couplings, the correlation coefficient is 0.985 and the alignment tensor parameters $D_a = 7.8$ and $R = 0.665$. For the D_{CH} values, the correlation coefficient is 0.980 and the alignment tensor parameters $D_a = 8.0$ and $R = 0.653$. Note, the displacement measured on a specific amide ^{15}N–^{1}H cross-peak corresponds to the coupling in its preceding amino acid residue.

It should be pointed out that the pulse sequences in Figs. 1A and B are only 2Δ longer than the 3D HNCO and HN(COCA)HA pulse sequences, respectively. Since $2\Delta = 9.5$ ms, the sensitivity of the proposed pulse sequences approaches that of 3D HNCO and HN(COCA)HA pulse sequences, respectively. Although the resonance lines in the ^{15}N dimension are broadened by the use of accordion principle, as demonstrated experimentally on the GB1 sample, the proposed experiments are very efficient and allow for easy and accurate determination of residual dipolar couplings.

In summary, sensitivity-enhanced IPAP experiments using the accordion principle were devised for measuring one-bond $^{13}C'$–$^{13}C^{\alpha}$ and $^{1}H^{\alpha}$–$^{13}C^{\alpha}$ residual dipolar couplings in proteins. The resolution of the resulting spectra is identical to that of the decoupled HSQC spectra. The sensitivity of the pulse sequences is slightly lower than that of the 3D HNCO and HN(COCA)HA pulse sequences given the additional delay of $2\Delta = 9.5$ ms. In addition, the precision of the measurements can be controlled by the digital resolution along the ^{15}N dimension. If the resolution of the 2D ^{15}N–$^{1}H^{N}$ HSQC spectrum is not sufficient, the present experiments can be easily transformed into 3D versions by introducing a poorly digitized third dimension. The most appealing

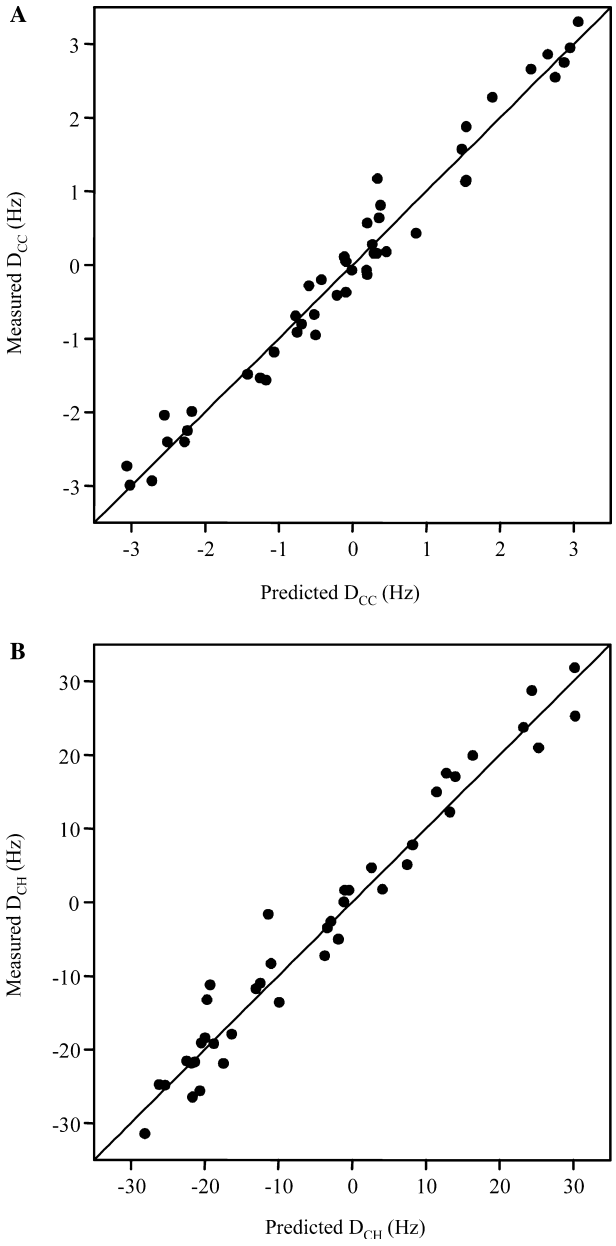

Fig. 3. Correlations between measured and predicted RDCs. (A) D_{CC} values and (B) D_{CH} couplings. For the D_{CC} values, the correlation coefficient is 0.985 and the alignment tensor parameters $D_a = 7.8$ and $R = 0.665$. For the D_{CH} values, the correlation coefficient is 0.980 and the alignment tensor parameters $D_a = 8.0$ and $R = 0.653$. Calculated RDCs were obtained using the refined NMR structure (PDB code: 3GB1) [22] as the model structure and the program SSIA [21].

feature of the experiments presented here is the ease and simplicity with which the dipolar couplings can be extracted. We believe that these experiments will find widespread application for determining one-bond $^{13}C'$–$^{13}C^{\alpha}$ and $^{1}H^{\alpha}$–$^{13}C^{\alpha}$ residual dipolar couplings in proteins.

Acknowledgments

This work was supported in part by the Intramural AIDS Targeted Antiviral Program of the Office of the Director of the National Institutes of Health to A.M.G.

References

[1] J.R. Tolman, J.M. Flanagan, M.A. Kennedy, J.H. Prestegard, Nuclear magnetic dipole interactions in field-oriented proteins: information for structure determination in solution, Proc. Natl. Acad. Sci. USA 92 (1995) 9279–9283.

[2] N. Tjandra, A. Bax, Direct measurement of distances and angles in biomolecules by NMR in a dilute liquid crystalline medium, Science 278 (1997) 1111–1114.

[3] E. deAlba, N. Tjandra, NMR dipolar couplings for the structure determination of biopolymers in solution, Prog. Nucl. Magn. Reson. Spectrosc. 40 (2002) 175–197.

[4] K. Ding, A.M. Gronenborn, Sensitivity-enhanced E.COSY-type HSQC experiments for accurate measurements of one-bond N-15-H-1(N) and N-15-C-13′ and two-bond C-13′-H-1(N) residual dipolar couplings in proteins, J. Magn. Reson. 158 (2002) 173–177.

[5] K. Ding, A.M. Gronenborn, Sensitivity-enhanced 2D IPAP, TROSY-anti-TROSY, and E.COSY experiments: alternatives for measuring dipolar N-15-H-1(N) couplings, J. Magn. Reson. 163 (2003) 208–214.

[6] K. Ding, A.M. Gronenborn, Simultaneous and accurate determination of one-bond N-15-C-13′ and two-bond H-1(N)-C-13′ dipolar couplings, J. Am. Chem. Soc. 125 (2003) 11504–11505.

[7] N. Tjandra, A. Bax, Large variations in C-13(alpha) chemical shift anisotropy in proteins correlate with secondary structure, J. Am. Chem. Soc. 119 (1997) 9576–9577.

[8] M. Ottiger, A. Bax, Determination of relative N-H-N N-C′, C-alpha-C′, and C(alpha)-H-alpha effective bond lengths in a protein by NMR in a dilute liquid crystalline phase, J. Am. Chem. Soc. 120 (1998) 12334–12341.

[9] D. Yang, J.R. Tolman, N.K. Goto, L.E. Kay, An HNCO-based pulse scheme for the measurement of C-13(alpha)-H-1(alpha) one-bond dipolar couplings in N-15, C-13 labeled proteins, J. Biomol. NMR 12 (1998) 325–332.

[10] D. Yang, R.A. Veners, G.A. Mueller, W.Y. Choy, L.E. Kay, TROSY-based HNCO pulse sequences for the measurement of (HN)-H-1-N-15, N-15-(CO)-C-13, (HN)-H-1-(CO)-C-13, (CO)-C-13-C-13(alpha) and (HN)-H-1-C-13(alpha) dipolar couplings in N-15, C-13, H-2-labeled proteins, J. Biomol. NMR 14 (1999) 333–343.

[11] A. Mittermaier, L.E. Kay, chi(1) torsion angle dynamics in proteins from dipolar couplings, J. Am. Chem. Soc. 123 (2001) 6892–6903.

[12] T.S. Ulmer, B.E. Ramirez, F. Delaglio, A. Bax, Evaluation of backbone proton positions and dynamics in a small protein by liquid crystal NMR spectroscopy, J. Am. Chem. Soc. 125 (2003) 9179–9191.

[13] A.G. Palmer III, J. Cavanagh, P.E. Wright, M. Rance, Sensitivity improvement in proton-detected 2-dimensional heteronuclear correlation NMR-spectroscopy, J. Magn. Reson. 93 (1991) 151–170.

[14] J. Cavanagh, A.G. Palmer III, P.E. Wright, M. Rance, Sensitivity improvement in proton-detected 2-dimensional heteronuclear relay spectroscopy, J. Magn. Reson. 91 (1991) 429–436.

[15] M. Ottiger, F. Delaglio, A. Bax, Measurement of J and dipolar couplings from simplified two-dimensional NMR spectra, J. Magn. Reson. 131 (1998) 373–378.

[16] G. Bodenhausen, R.R. Ernst, The accordion experiment, a simple approach to 3-dimensional NMR-spectroscopy, J. Magn. Reson. 45 (1981) 367–373.

[17] G. Bodenhausen, R.R. Ernst, Direct determination of rate constants of slow dynamic processes by two-dimensional accordion spectroscopy in nuclear magnetic resonance, J. Am. Chem. Soc. 104 (1982) 1304–1309.

[18] M. Piotto, V. Saudek, V. Sklenar, Gradient-tailored excitation for single-quantum NMR-spectroscopy of aqueous-solutions, J. Biomol. NMR 2 (1992) 661–665.

[19] A.M. Gronenborn, D.R. Filpula, N.Z. Essig, A. Achari, M. Whitlow, P.T. Wingfield, G.M. Clore, A novel, highly stable fold of the immunoglobulin binding domain of streptococcal protein-G, Science 253 (1991) 657–661.

[20] F. Delaglio, S. Grzesiek, G.W. Vuister, G. Zhu, J. Pfeifer, A. Bax, NMRPipe, a multidimensional spectral processing system based on Unix pipes, J. Biomol. NMR 6 (1995) 277–293.

[21] M. Zweckstetter, A. Bax, Prediction of sterically induced alignment in a dilute liquid crystalline phase: aid to protein structure determination by NMR, J. Am. Chem. Soc. 122 (2000) 3791–3792.

[22] J. Kuszewski, A.M. Gronenborn, G.M. Clore, Improving the packing and accuracy of NMR structures with a pseudopotential for the radius of gyration, J. Am. Chem. Soc. 121 (1999) 2337–2338.